## ELECTROCHEMISTRY

# Lithium-compatible and air-stable vacancy-rich $Li_9N_2Cl_3$ for high–areal capacity, long-cycling all–solid-state lithium metal batteries

Weihan Li[1,2]†, Minsi Li[1,2]†, Po-Hsiu Chien[3]†, Shuo Wang[4]†, Chuang Yu[1], Graham King[5], Yongfeng Hu[5], Qunfeng Xiao[5], Mohsen Shakouri[5], Renfei Feng[5], Bolin Fu[1], Hamidreza Abdolvand[1], Adam Fraser[1], Ruying Li[1], Yining Huang[3], Jue Liu[3]*, Yifei Mo[4,6]*, Tsun-Kong Sham[2]*, Xueliang Sun[1,7]*

Attaining substantial areal capacity (>3 mAh/cm$^2$) and extended cycle longevity in all–solid-state lithium metal batteries necessitates the implementation of solid-state electrolytes (SSEs) capable of withstanding elevated critical current densities and capacities. In this study, we report a high-performing vacancy-rich $Li_9N_2Cl_3$ SSE demonstrating excellent lithium compatibility and atmospheric stability and enabling high–areal capacity, long-lasting all–solid-state lithium metal batteries. The $Li_9N_2Cl_3$ facilitates efficient lithium-ion transport due to its disordered lattice structure and presence of vacancies. Notably, it resists dendrite formation at 10 mA/cm$^2$ and 10 mAh/cm$^2$ due to its intrinsic lithium metal stability. Furthermore, it exhibits robust dry-air stability. Incorporating this SSE in Ni-rich $LiNi_{0.83}Co_{0.11}Mn_{0.06}O_2$ cathode-based all–solid-state batteries, we achieve substantial cycling stability (90.35% capacity retention over 1500 cycles at 0.5 C) and high areal capacity (4.8 mAh/cm$^2$ in pouch cells). These findings pave the way for lithium metal batteries to meet electric vehicle performance demands.

## INTRODUCTION

Lithium-ion rechargeable batteries (LIBs) have revolutionized consumer electronics in recent decades and are becoming increasingly prevalent in energy storage and power applications globally (*1*). For high-performance application in electric vehicles (EVs), LIBs require sufficient energy density to achieve long driving range that matches or exceeds that of gasoline cars, as well as high safety and long cycle life. Lithium metal batteries are widely considered as promising cells to achieve energy densities above 350 Wh/kg and up to 500 Wh/kg when using high-capacity cathode materials and lithium metal anodes (*2*). Among the commercially available cathode materials, lithium nickel manganese cobalt oxide (NMC) cathodes demonstrate high capacity (≥200 mAh/g) and high operating voltage, which enables high areal capacity of >3 mAh/cm$^2$ (*3*). Lithium metal is recognized as the ultimate anode candidate because of its high theoretical capacity (3860 mAh/g), low electrochemical potential (−3.040 V versus standard hydrogen electrode), and low density (0.59 g/cm) (*4*). However, the safety concerns and fast decay owing to lithium dendrite growth, dead lithium, and fast-growing solid electrolyte interphase overshadow the promising electrochemical performance (*5*). Emerging all–solid-state lithium

metal batteries have the potential to achieve high specific energy, long cycling life, and high safety by replacing the flammable liquid electrolytes in conventional LIBs with solid-state electrolytes (SSEs) (*6–9*). Some crucial challenges remain unsolved in the practical application of sulfide, halide, and oxide SSEs in all–solid-state lithium metal batteries. Because of their unstable characteristics, sulfides and halides suffer from serious interfacial side reactions when contacting lithium metal (*10*, *11*). In the case of oxides, the high electronic conductivity of grain boundaries results in propagation of lithium dendrites, especially at high current densities (*12*, *13*). As a result, low Coulombic efficiency (CE), rapid capacity fade, and even battery failure are typically observed (*14–17*).

It is crucial to develop rational strategies to overcome the interfacial challenges posed by SSEs. While coating lithium metal with a thin protection layer can be a temporary remedy, the ultimate solution is to develop lithium-compatible SSEs that satisfy low resistance for lithium-ion diffusion and high stability toward lithium metal during many stripping/platting cycles at high current densities (*18*, *19*). Among the developed SSEs and others predicted by theoretical calculations, nitrides are promising candidates that can stabilize lithium metal anodes (*20–22*). Until now, several nitride SSEs have been developed, such as lithium phosphorus oxynitride (*23*), lithium nitrides containing carbon elements (e.g., $Li_2CN_2$) (*24*), lithium silicon nitrides (*25*), and lithium nitride halides (*21*, *22*). While thin-film all–solid-state lithium metal batteries fabricated by the sputtering deposition method using LiPON demonstrated excellent cycling performance (*26*), no study reports practical bulk all–solid-state lithium metal batteries with long cycling life (>1000 cycles) using nitride SSEs. A plausible explanation is sluggish diffusion of lithium ions in reported nitride SSEs and nitride SSE–lithium interfaces, which relies on the lithium vacancy defects as predicted by theoretical calculations and confirmed by

[1]Department of Mechanical and Materials Engineering, Western University, London, ON N6A 5B9, Canada. [2]Department of Chemistry and Soochow-Western Centre for Synchrotron Radiation Research, Western University, London, ON N6A 5B7, Canada. [3]Neutron Scattering Division, Oak Ridge National Laboratory, Oak Ridge, TN 37831, USA. [4]Department of Materials Science and Engineering, University of Maryland, College Park, MD 20742, USA. [5]Canadian Light Source, 44 Innovation Boulevard, Saskatoon, SK S7N 2V3, Canada. [6]Maryland Energy Innovation, University of Maryland, College Park, MD 20742, USA. [7]Eastern Institute for Advanced Study, Eastern Institute of Technology, Ningbo, Zhejiang 315200, P.R. China.
*Corresponding author. Email: xsun9@uwo.ca (X.S.); tsham@uwo.ca (T.-K.S.); yfmo@umd.edu (Y.M.); liuj1@ornl.gov (J.L.)
†These authors contributed equally to this work.

experimentation (*16*, *27*, *28*). Therefore, it is rational to design and tune the vacancy defects in nitrides to improve stability toward lithium metal, especially under high current densities and with high areal capacities. In the present work, we developed a lithium nitride halide SSE, $Li_9N_2Cl_3$, which presents high chemical stability toward lithium metal and demonstrate in high–areal capacity and long-cycling all–solid-state lithium metal batteries.

Here, we report a vacancy-rich $Li_9N_2Cl_3$ SSE with high lithium compatibility and high air stability, construct stable lithium-SSE interfaces, and demonstrate high–areal capacity, long-cycling all–solid-state lithium metal batteries. The vacancy-rich $Li_9N_2Cl_3$ SSE exhibits an elevated room-temperature ionic conductivity of $4.3 \times 10^{-5}$ S/cm, surpassing previously reported counterparts by an order of magnitude (*21*). Through rigorous analysis using synchrotron-based x-ray diffraction (SXRD), pair distribution function (PDF), time-of-flight (TOF) neutron diffraction, and density functional theory (DFT) calculation and ab initio molecular dynamics (AIMD) simulation, a lattice and vacancy-driven lithium-ion conduction mechanism is identified. Notably, this vacancy-rich $Li_9N_2Cl_3$ SSE facilitates high critical current densities (CCDs) and lithium-stripping/plating capacities (10 mA/cm$^2$ and 10 mAh/cm$^2$, respectively) while exhibiting ultrastable cycling performance for over 2000 cycles at 1.0 mA/cm$^2$ and 1.0 mAh/cm$^2$. This impressive lithium compatibility, which mitigates interfacial reactions and Li dendrite formation, was revealed through in-depth operando studies involving SXRD, x-ray absorption near-edge structure (XANES), and DFT calculations. The notable dry-air stability of this vacancy-rich $Li_9N_2Cl_3$, confirmed via in situ and operando XANES and SXRD studies, substantiates its potential for commercial applications. Because of the high lithium compatibility of $Li_9N_2Cl_3$, we demonstrate an all–solid-state lithium metal battery design that showed extremely high cycling stability (90.35% capacity retention with 103 mAh/g over 1500 cycles at 0.5 C) and delivered high areal capacity of ~5.16 mAh/cm$^2$ (cathode loading of 27.42 mg/cm$^2$) for small-area pellet type cells (size, 0.785 cm$^2$; thickness of SSE, ~0.55 mm) and 4.8 mAh/cm$^2$ (cathode loading of 27.42 mg/cm$^2$) for all–solid-state lithium metal pouch cells (size, 2 cm by 2.5 cm; thickness of SSE, ~200 μm).

## RESULTS

### Morphology characterization and ionic conductivity

High-energy ball milling a mixture of $Li_3N$ and LiCl with a molar ratio of 2:3 yielded this vacancy-rich $Li_9N_2Cl_3$. A series of $Li_9N_2Cl_3$ SSEs were prepared by varying the ball-milling speeds from 200 to 700 rpm and milling durations from 2 to 70 hours. These samples are designated as $Li_9N_2Cl_3$-*A*rpm-*B*h, where *A* represents the milling speed and *B* represents the milling duration. Figure 1A shows the XRD patterns during the structural transformation with a constant milling speed of 500 rpm. Increasing ball-milling time from 2 to 24 hours resulted in the gradual formation of pure $Li_9N_2Cl_3$ crystals. Then, lithium-ion conductivity of $Li_9N_2Cl_3$ was evaluated by the ac impedance method using pressed pellets. Figure S1 (see the Supplementary Materials) summarizes the ionic conductivity at room temperature (25°C) and the activation energy as a function of ball-milling time. Among the prepared SSEs, $Li_9N_2Cl_3$-500 rpm-24 hours demonstrated the highest room-temperature ionic conductivity of $4.3 \times 10^{-5}$ S/cm, which is around one order of magnitude than that previously reported using

the annealing method ($1.07 \times 10^{-6}$ S/cm) (*21*) and higher than that of commercial LiCl, LiI, and $Li_3N$ (LiCl, $7.33 \times 10^{-11}$ S/cm; LiI, $2.22 \times 10^{-7}$ S/cm; and $Li_3N$, $1.86 \times 10^{-5}$ S/cm) (fig. S2, see the Supplementary Materials). In addition, the influence of ball-milling speed on the crystal structures and lithium-ion diffusion was examined over a range of ball-milling speed (i.e., 200, 300, 400, 500, 600, and 700 rpm), maintaining a constant ball-milling duration of 24 hours as shown in figs. S1, S3, and S4 (see the Supplementary Materials). At milling speeds of 200 and 300 rpm, no discernible reaction between $Li_3N$ and LiCl was observed. However, milling speeds ranging from 400 to 700 rpm proved conducive for the synthesis of $Li_9N_2Cl_3$. Notably, the ball-milling condition of 500 rpm for 24 hours was identified as the optimal parameter, yielding the highest ionic conductivity at room temperature. Figure 1B shows the corresponding Arrhenius plot. The activation energy (0.378 eV) is lower than that previously reported (0.49 eV) (*21*). Unlike temperature-dependent impedance that can reflect ionic dynamics contribution from the bulk materials, grain boundaries, and other interfaces in the sample, nuclear magnetic resonance (NMR) spectroscopy can selectively probe ion motions on a much shorter diffusion length scales in the bulk. We used temperature-dependent $^7Li$ spin-lattice relaxation time ($T_1$) of the prepared $Li_9N_2Cl_3$-500 rpm-24 hours to quantify the intrinsic lithium-ion dynamics and the corresponding energy barrier. The spin-lattice relaxation time of $Li_9N_2Cl_3$-500 rpm-24 hours was 0.11 s at room temperature. However, the $1/T_1$ of $Li_9N_2Cl_3$-500 rpm-24 hours does not reach the maximum due to the temperature limitations of the instrument used for this work. The $1/T_1$ exhibited a typical Arrhenius behavior with an activation energy of 0.13 eV for $Li_9N_2Cl_3$-500 rpm-24 hours as shown in Fig. 1C. The lower activation energy compared to that deduced from temperature-dependent ionic conductivity (0.13 eV versus 0.378 eV) suggests that a much faster lithium-ion mobility exists in the local diffusion length scales of Li9N2Cl3-500 rpm-24 hours and existing grain boundaries in the pressed pellets. In addition, the electronic conductivity of $Li_9N_2Cl_3$-500 rpm-24 hours was tested using the dc polarization method. As shown in fig. S5 (see the Supplementary Materials), the dc polarization curves at 0.1, 0.2, 0.3, 0.4, and 0.5 V show initial fast-decay current and stabilize at around $10^{-9}$ A after 1 hour. On the basis of the linear fit of stable response current as a function of voltage, the dc electronic conductivity of $Li_9N_2Cl_3$-500 rpm-24 hours is around $1.7 \times 10^{-9}$ S/cm. The dc electronic conductivity is around five orders of magnitude lower than the ionic conductivity, suggesting the pure ionic conducting characteristic of $Li_9N_2Cl_3$-500 rpm-24 hours.

The mechanism of higher ionic conductivity in ball milled versus annealed $Li_9N_2Cl_3$ was investigated through the influence of heat treatment on ball-milled $Li_9N_2Cl_3$. As shown in fig. S1 (see the Supplementary Materials), $Li_9N_2Cl_3$-500 rpm-24 hours was heat-treated up to 450°C. Heating to 250°C led to the formation of another phase, $Li_4NCl$, which is expected to provide lower ionic conductivity (*29*). Heating to between 150° and 200°C maintained the $Li_9N_2Cl_3$ crystal structure but with decreased lattice parameters and lower ionic conductivity, as shown in fig. S1 (see the Supplementary Materials). Because the lithium-ion diffusion in $Li_9N_2Cl_3$ crystals relies on lithium transport between the lithium vacancy sites (as discussed in detail in the next section), decreased lattice parameters present a higher barrier to lithium transport, increase the diffusion gap energy, and lower the ionic conductivity (*22*, *30*). The morphology of $Li_9N_2Cl_3$ SSEs prepared by ball milling was
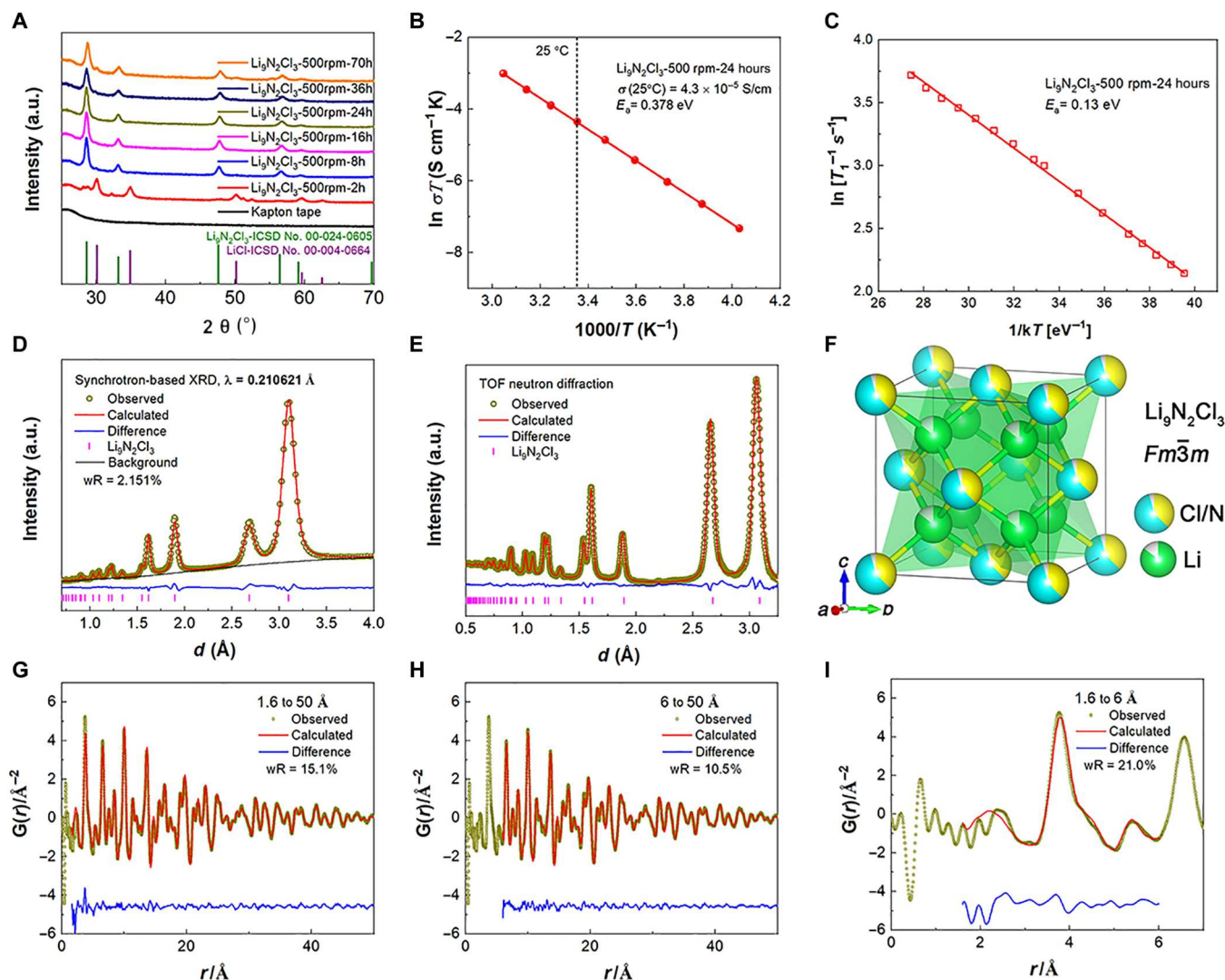
**Fig. 1. Crystal structure and local disorder characterization and lithium-ion diffusion properties.** (**A**) The x-ray powder diffraction patterns of $Li_9N_2Cl_3$ as a function of the ball-milling time, (**B**) Arrhenius plots, and (**C**) temperature-dependent $^7Li$ spin-lattice relaxation time ($T_1$) changes of vacancy-rich $Li_9N_2Cl_3$; (**D**) SXRD pattern and corresponding Rietveld refinement and (**E**) TOF neutron diffraction data (Bank 3) and corresponding Rietveld refinement, and (**F**) calculated crystal structure of vacancy-rich $Li_9N_2Cl_3$, $Li^+$ (cyan), $N^{3-}$ (yellow), and $Cl^-$ (green). (**G** to **I**) PDF $G(r)$ of $Li_9N_2Cl_3$ and fit for corresponding $G(r)$ for different $r$ ranges. a.u., arbitrary units; h, hours.

studied by scanning electron microscopy (SEM) and showed typical polyhedral particles (fig. S6, see the Supplementary Materials) with long dimensions ranging from 100 nm to 3 μm. As ball-milling duration extends from 16 to 70 hours, with a consistent milling speed of 500 rpm, there is a noticeable decline in particle size. Similarly, with a fixed milling time of 24 hours, particle size diminishes as milling speeds increase from 400 to 700 rpm. Specifically, at a milling speed of 500 rpm, the primary particle size range narrows from 500 to 900 nm to 100 to 400 nm as milling durations lengthen from 16 to 24 hours. Beyond this, from 24 to 70 hours, the proportion of particles within the 100- to 400-nm range rises from 51.7 to 64.1%. For a 24-hour milling period at a reduced speed of 400 rpm, the prevailing particle size enlarges, settling within the 0.6- to 1.4-μm bracket. Conversely, as milling speeds escalate from 500 to 700 rpm, the dominant particle size contracts to 100 to 400 nm, and its frequency increases, spanning from 51.7 to 61.1%.

## Crystal structure and local disorder

The crystal structure and local disorder of $Li_9N_2Cl_3$ were studied by SXRD, TOF neutron powder diffraction, and x-ray total scattering. Figure 1 (D and E) and figs. S4 and S7 (see the Supplementary Materials) show the SXRD pattern and TOF neutron power diffraction data of a series of $Li_9N_2Cl_3$ SSEs. These SSEs were synthesized under varied ball-milling parameters, with speeds ranging from 200 to 700 rpm and durations extending from 2 to 70 hours. The corresponding crystal structure of $Li_9N_2Cl_3$-500 rpm-24 hours was refined using the Rietveld method as shown in Fig. 1F. The detailed structural and Rietveld refinement information of these $Li_9N_2Cl_3$ SSEs are shown in tables S1 to S15 (see the Supplementary Materials). Ball-milled $Li_9N_2Cl_3$ is determined to have a defect anti-fluorite structure with cubic symmetry (space group, $Fm\bar{3}m$) and lattice parameter $a = 5.3506$ (3) Å. In the ball-milled $Li_9N_2Cl_3$ samples with a constant milling speed of 500 rpm, the concentration of vacancies

for lithium, nitrogen, and chloride typically increases with milling time, peaking at 24 hours. However, this concentration declines when the milling duration extends to 36 and 70 hours, as shown in fig. S9A (see the Supplementary Materials). The impact of varying milling speeds—specifically, 400, 500, 600, and 700 rpm—on vacancy concentrations within the ball-milled $Li_9N_2Cl_3$ was assessed and is depicted in fig. S9B (see the Supplementary Materials). Maintaining a consistent milling duration of 24 hours, the concentration of vacancies for lithium, nitrogen, and chloride in the $Li_9N_2Cl_3$ samples also peaks for the $Li_9N_2Cl_3$-500 rpm-24 hours sample. The $Li_9N_2Cl_3$-500 rpm-24 hours sample, denoted as vacancy-rich $Li_9N_2Cl_3$, exhibited the maximum vacancy concentrations as $Li^+$ occupies tetrahedral sties [$Li(N/Cl)_4$ tetrahedra] with 14.0(5)% vacancy, and $N^{3+}$ and $Cl^-$ ions take the vertex sites of the $Li(N/Cl)_4$ tetrahedral randomly with the atomic ratio of 2:3 and 4.5(5)% vacancy. This formation of vacancies in $Li_9N_2Cl_3$ is due to the crystal structure. The formation energy of single lithium vacancy in this vacancy-rich $Li_9N_2Cl_3$, β-$Li_3N$ (2b and 4f sites), and LiCl was calculated by the DFT method as shown in fig. S10A (see the Supplementary Materials) [31, 32]. The mean lithium vacancy formation energy in this vacancy-rich $Li_9N_2Cl_3$ is ~1.31 eV, which is much lower than that of LiCl (4.82 eV) and close to that of β-$Li_3N$ [0.81 eV for Li (4f) sites and 1.43 for Li (2b) sites]. Therefore, the high-energy ball-milling process enables vacancy-rich structures in $Li_9N_2Cl_3$ crystal structures. However, the defect concentration in crystals has an upper limit ~14.0(5)% for $Li_9N_2Cl_3$-500 rpm-24 hours due to the tolerance factor. Upon analyzing the correlations between lithium-ion diffusion properties (i.e., room-temperature ionic conductivity and activation energy), vacancy concentration, and particle size as illustrated in figs. S1, S6, and S9 (see the Supplementary Materials), it becomes evident that an elevated vacancy concentration primarily contributes to the enhanced lithium-ion diffusion observed in in the $Li_9N_2Cl_3$ SSEs. The high concentration of vacancies [14.0(5)%] in the lithium sublattice determines the fast lithium diffusion between adjacent tetrahedral sites and realizes higher ionic conductivity [21]. The lithium diffusion behavior in vacancy-rich $Li_9N_2Cl_3$ was further studied by AIMD simulation as shown in fig. S10B (see the Supplementary Materials) [33, 34]. Fast lithium diffusion is observed in these vacancy-rich structures with the activation energy of 0.41 eV and ionic conductivity of $6.0 \times 10^{-5}$ S/cm at 300 K, which is consistent with our experimental results and suggests that the defects and disorder structures accelerate lithium diffusion [35].

In addition to the crystal structure, the local disorder was studied by x-ray total scattering. The PDF $G(r)$ of this vacancy-rich $Li_9N_2Cl_3$ is shown in fig. S8 (see the Supplementary Materials) along with the PDF analysis results in Fig. 1 (G to I) and displays interatomic distances in real space that is consistent with the refined average crystal structure in Fig. 1F. Detailed PDF fit results can be found in table S3 (see the Supplementary Materials). Starting from the refined crystal structure in Fig. 1F, the PDF fit result for the $r$ range of 1.6 to 50 Å shows relatively large difference [weighted residual (wR) = 15.1%] compared with the experimental result. This result indicates high local displacements inside the prepared materials, as shown in Fig. 1G. The PDF fit was split into two ranges: 1.6 to 6.0 Å (Fig. 1H) and 6.0 to 50 Å (Fig. 1I). The first range corresponds to one unit cell, and the second range represents supercell. As expected, the fit result for the $r$ range of 6.0 to 50 Å presents better agreement with experimental data with a smaller difference (wR =

10.5%). This indicates that the atomic displacement, i.e., static disorder, is averaged out over the spatial distribution during data collection. Hence, the refined crystal structure by PDF is consistent with that obtained by the Rietveld refinement of SXRD. However, as shown in Fig. 1 (H and I), noticeable difference exists between experimental data and fit result in the $r$ range of 1.6 to 6.0 Å when $G(r)$ is refined against the real space from 1.6 to 50 Å, suggesting that the level of static disorder quickly quenches beyond one unit cell. The peak at 1.97 Å is a termination ripple as there should not be any interatomic distance in the crystal structure of this vacancy-rich $Li_9N_2Cl_3$. The first informative peak corresponding to molecular bonds is at ~2.37 Å, displaying the Li-N/Cl interatomic distance, which is broad and represents a distribution of bond lengths. The nearest neighboring Li-Li interatomic distance is around 2.7 Å, although the peaks are small with a slight shoulder on the peak at 2.4 Å. Another peak at 3.8 Å corresponds to the interatomic distance of Cl/N-Cl/N. Evidently, there is a notable difference between the experimental and calculated Li-N/Cl interatomic distance (the calculated value is ~2.24 Å). This is due to the longer Li-Cl interatomic distance compared to Li-N, owing to stronger scattering of $Cl^-$, higher element content of $Cl^-$ than $N^{3-}$ and larger radius of $Cl^-$ compared to $N^{3-}$. The longer Li—Cl bonds cause the peak to shift to higher $r$, while the Li-N contribution generates a small shoulder at low $r$. This kind of local displacement also occurs with Cl/N—Cl/N bonds. Compared with the perfect average crystal structure, the local disorder in Li—N/Cl bonds and Cl/N—Cl/N bonds means that N and Cl should not randomly occupy the vertex sites of $Li(N/Cl)_4$ tetrahedra after comparing the local and global structures.

## Chemical stability toward lithium metal
Previous theoretical investigations have predicted that $Li_9N_2Cl_3$ is chemically stable toward Li metal [20, 36, 37]. To study this chemical stability at the SSE-Li interfaces, SXRD and XANES with low-angle (3°) incidence x-ray were used, taking advantage of shallow probing depths [38]. As shown in Fig. 2A, modified coin cells with a window consisting of Mylar film were used as cells in operando SXRD and XANES studies. In detail, a pressed vacancy-rich $Li_9N_2Cl_3$ pellet was sandwiched by two pieces of Li metal and placed in the operando cell using springs and spacers to generate tight contact between the SSE and Li metal. During the operando SXRD and XANES studies, x-rays with low-incidence angle (3°) pass through the Mylar film window and Li metal, the scattered x-rays and fluorescent x-rays were collected by one Pilatus pixel area detector and one fluorescence detector, respectively. The crystal structure evolution and chemical information at the SSE-Li interface can be evaluated.

Figure 2B shows the operando SXRD study result. The pristine SXRD pattern shows a mixture of crystal patterns belonging to $Li_9N_2Cl_3$ and Li metal with no additional peaks. After ~8 hours, the SXRD patterns relatively unchanged, indicating no formation of additional crystalline phases at the vacancy-rich $Li_9N_2Cl_3$-Li interface. To detect the possible formation of amorphous phases at the interface, XANES was performed, which is sensitive to the evolution of chemical and electronic structure, as shown in Fig. 2 (C to E). Figure 2D shows the operando XANES spectra at the Cl K-edge. The pristine sample presents the main absorption edge with the white line peaks at ~2826.0 and ~2828.7 eV, due to the electron transition from the 1 s orbitals to 4p orbitals. Contact between
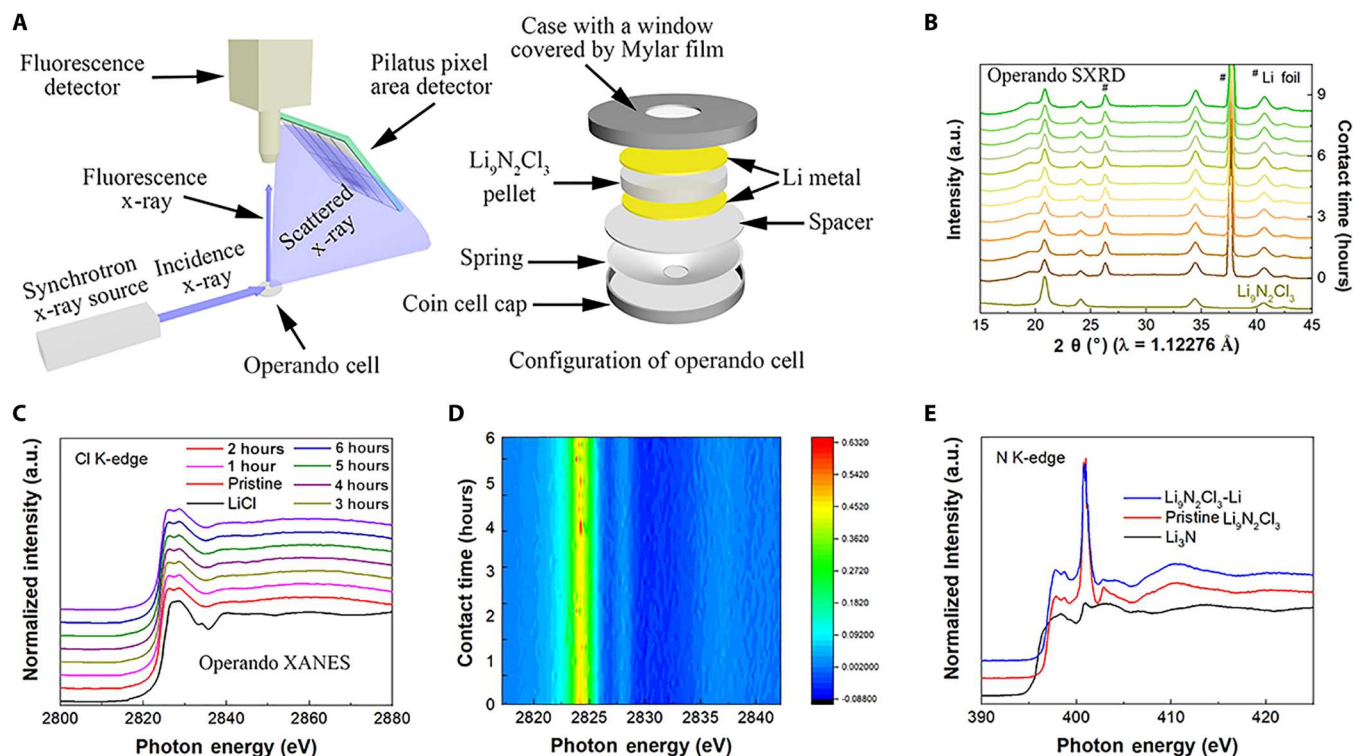
**Fig. 2. Operando SXRD and XANES studies of chemical stability toward lithium metal.** (**A**) Schematic illustration of the operando SXRD and XANES studies of chemical stability of vacancy-rich $Li_9N_2Cl_3$ upon contact with Li metal and the configuration of the operando cell. (**B**) Operando SXRD pattern evolution and (**C**) XANES spectra at Cl K-edge with (**D**) first derivative mapping of $Li_9N_2Cl_3$ during contact with Li metal for several hours. (**E**) N K-edge XANES spectra comparison of $Li_9N_2Cl_3$ before and after contact with Li metal.

the vacancy-rich $Li_9N_2Cl_3$ pellet and Li metal for 6 hours resulted in no feature change in the XANES (Fig. 2C and fig. S11). In addition, the first derivative mapping (Fig. 2D) of the Cl K-edge confirmed that no additional XANES feature was formed during the 6 hours. Moreover, ex situ N K-edge XANES study showed no change between the pristine SSE powder and the SSE after contact with Li metal. Combining the operando SXRD and XANES results, we conclude that $Li_9N_2Cl_3$ is chemically stable toward Li metal during tight contact process.

The chemical stability of this vacancy-rich $Li_9N_2Cl_3$ SSE toward Li metal was further confirmed by carrying out operando XANES during the lithium-plating and stripping processes (Fig. 3). As shown in Fig. 3A, operando XANES study was performed in one vacuum x-ray absorption spectroscopy chamber using the same operando cell as used above. Because of the low angle of incidence x-rays, the fluorescent x-rays mainly come from the interfaces that are the interesting areas. Figure 3C shows the discharge/charge voltage profiles during lithium plating and stripping at current densities of 0.1, 0.2, 0.3, and 0.4 mA/cm$^2$ with 1 hour plating/stripping time. During plating and stripping processes, XANES was collected in real time. Several typical lithium-plating and lithium-stripping states are marked in Fig. 3C, and the corresponding XANES spectra at Cl K-edge are displayed in Fig. 3B. There is no feature evolution during the total 8 hours of plating and stripping processes. The first derivative mapping for the XANES feature evolution during the overall process also shows no feature evolution as shown in Fig. 3D, indicating intrinsic stability of this vacancy-rich

$Li_9N_2Cl_3$ toward lithium metal. This stability is further corroborated by nanoindentation testing as shown in fig. S12 (see the Supplementary Materials), which reveals a Young's modulus ($E = 42.43$ GPa) of this vacancy-rich $Li_9N_2Cl_3$ greater than the bulk Young's modulus ($E = 7.8$ GPa) of lithium metal (*39, 40*). This high Young's modulus underlines its ability to prevent lithium dendrite growth.

## Air stability study by operando SXRD and in situ XANES

Air stability or dry-air stability is an important characteristic in the practical application of SSEs for large-scale manufacturing of solid-state batteries (*41*). Operando SXRD and in situ XANES were used to confirm the chemical stability of this vacancy-rich $Li_9N_2Cl_3$ toward dry air as shown in Fig. 4 (*42*). Figure 4A shows the operando SXRD study of the crystal structure evolution of this vacancy-rich $Li_9N_2Cl_3$ upon exposure to ambient air. The collection time for each pattern is around 10 min. This pristine vacancy-rich $Li_9N_2Cl_3$ was initially covered by Kapton tape to prevent the decomposition in ambient air with humidity of ~20%. SXRD patterns were then collected after $Li_9N_2Cl_3$ was exposed to ambient air by cutting the Kapton tape with a slit. Several additional XRD peaks were observed that gradually increased intensity with the exposure time. Exposing to ambient air for ~140 min results in mixed phases of $Li_9N_2Cl_3$ and by-products, indicating chemical instability in ambient air. The compositions of by-products are further confirmed by analyzing the reaction products between $Li_9N_2Cl_3$ and deionized water by XRD as the following in situ XANES results suggest that moisture results in decomposition (fig. S13, see the Supplementary
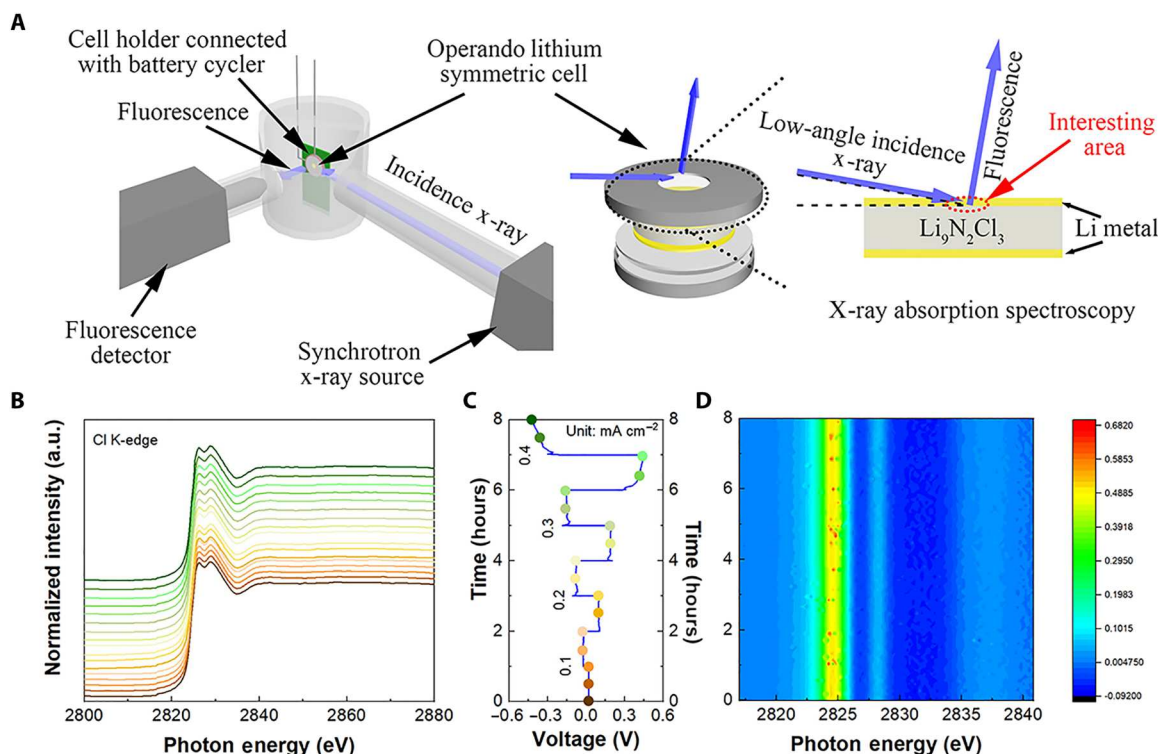
**Fig. 3. Operando XANES studies of chemical stability toward lithium metal.** (**A**) Schematic illustration of the operando XANES studies of chemical stability of vacancy-rich $Li_9N_2Cl_3$ during lithium-plating/stripping process and the configuration of the operando cell for XANES. (**B**) Operando XANES spectra at Cl K-edge with (**C**) the corresponding discharge/charge voltage profiles of the Li cycling in the operando cell at several current densities (i.e., 0.1, 0.2, 0.3, and 0.4 mA cm$^{-2}$) and (**D**) with first derivative mapping of vacancy-rich $Li_9N_2Cl_3$ during lithium-plating/stripping process.

Materials). The gas by-product is $NH_3$, and the solid by-products are $Li_4Cl(OH)_3$ and $NH_4Cl$. The reaction between $Li_9N_2Cl_3$ and moisture is confirmed as below

$$4\ Li_9N_2Cl_3 + 27\ H_2O(g) = 9\ Li_4(OH)_3Cl + 3\ NH_4Cl + 5\ NH_3(g)$$
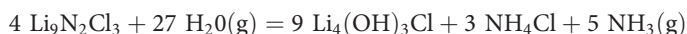
The chemical stability of this vacancy-rich $Li_9N_2Cl_3$ toward dry air was studied by in situ XANES carried out using several specific gases, including ambient air, mixture of dry air and moisture, dry air, and mixture of Ar and moisture (*42*). The vacancy-rich $Li_9N_2Cl_3$ samples were first stored in one XANES chamber filled with He gas to prevent the influence of ambient air outside of chamber. Then, the test gases were introduced to the chamber and to expose the vacancy-rich $Li_9N_2Cl_3$ sample to these gases. After a controlled time, the chamber was purged with He gas for at least 10 min to remove all test gases (e.g., air, Ar, or moisture). After this purge with He, the Cl K-edge XANES spectrum evolution with the exposure time was collected using the fluorescence yield (FLY) mode. Figure 4B shows the Cl K-edge XANES spectrum evolution upon exposure to ambient air. After exposure to ambient air for 5 min and up to 2 hours, one additional peak at 2827.7 eV was observed, related to the formation of two additional phases [$Li_4(OH)_3Cl$ and $NH_4Cl$] confirmed in operando SXRD study. The same in situ XANES studies were performed with other target gases (i.e., mixture of dry air and moisture, dry air, and mixture of Ar and moisture). As shown in Fig. 4 (C to E) and fig. S14 (see the Supplementary Materials), the mixture of dry air and moisture and the mixture of Ar and moisture lead to the same decomposition of

this vacancy-rich $Li_9N_2Cl_3$ as seen with ambient air. However, this vacancy-rich $Li_9N_2Cl_3$ shows extremely chemical stability in dry air, as shown in Fig. 4D and fig. S14. This indicates that moisture leads to the decomposition of $Li_9N_2Cl_3$ in ambient air, which is further studied by ex situ N K-edge XANES studies as shown in fig. S15 (see the Supplementary Materials). The N K-edge XANES spectra maintain almost the same during exposure to dry air, suggesting excellent chemical stability of $Li_9N_2Cl_3$ in dry air. In addition, the main features at ~397.9 eV undergo evolution during exposure to ambient air, the mixture of Ar and moisture, and the mixture of dry air and moisture, confirming the serious reaction between $Li_9N_2Cl_3$ with moisture and the formation of by-products of $NH_4Cl$ (*43*). When exposing $Li_9N_2Cl_3$ to the atmosphere in dry rooms with low dew points of around −50° to −60°C (<0.3% relative humidity), the ionic conductivity of this vacancy-rich $Li_9N_2Cl_3$ is preserved at around $4.15 \times 10^{-5}$ S/cm during exposures up to 200 hours (Fig. 4F). Even when the relative humidity increased to around 3 to 5%, it can still maintain at around $3.65 \times 10^{-5}$ S/cm after exposure for 200 hours. The excellent chemical stability in dry room makes this vacancy-rich $Li_9N_2Cl_3$ promising for large-scale manufacturing applications in battery dry rooms without the required use of inert atmosphere glove boxes.

## Electrochemical performance of lithium symmetric cells and all–solid-state lithium metal batteries

As discussed in Fig. 5, most common SSEs are instable against lithium metal anodes, including oxynitride, oxides, sulfides, and
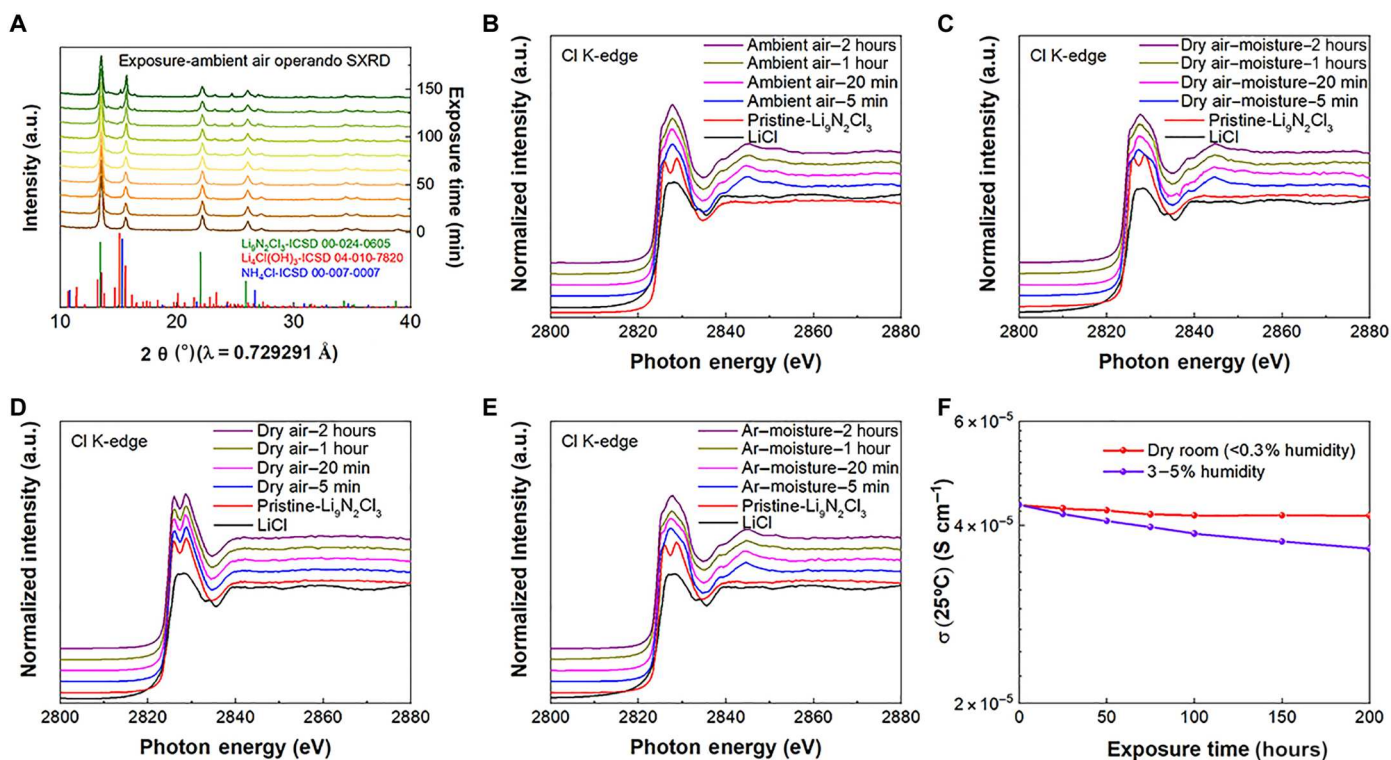
**Fig. 4. Air stability studies of this vacancy-rich Li₉N₂Cl₃ SSE.** (**A**) Operando SXRD patterns of this vacancy-rich Li$_9$N$_2$Cl$_3$ SSE during exposure process to ambient air for 140 min. In situ Cl K-edge XANES studies of this vacancy-rich Li$_9$N$_2$Cl$_3$ SSE during exposure process to (**B**) ambient air, (**C**) the mixture of dry air and moisture, (**D**) dry air, and (**E**) the mixture of Ar and moisture for 2 hours. (**F**) The lithium-ion conductivity evolution at 25°C of this vacancy-rich Li$_9$N$_2$Cl$_3$ SSE upon exposure to dry air.

chlorides. In contrast, this vacancy-rich Li$_9$N$_2$Cl$_3$ shows unique stability in contact with lithium metal. However, its anodic limit is only up to 0.5 V, and the oxidation of N$^{3-}$ ions would happen at increase voltage (fig. S16A, see the Supplementary Materials). In summary, the phase equilibrium calculation result not only confirms that this vacancy-rich Li$_9$N$_2$Cl$_3$ is compatible with Li metal but also indicates that this vacancy-rich Li$_9$N$_2$Cl$_3$ would decompose at higher applied voltage. Therefore, the reasonable working full-battery configuration needs an SSE that had high room-temperature ionic conductivity and compatibility with vacancy-rich Li$_9$N$_2$Cl$_3$ SSE and the cathodes. The cathode-compatible Li$_{2.73}$Ho$_{1.09}$Cl$_6$ SSE was used to couple cathode materials, which presents high room-temperature ionic conductivity of $4.78 \times 10^{-4}$ S/cm with the activation energy of 0.42 eV (fig. S17, see the Supplementary Materials) (*44*). The Li$_{2.73}$Ho$_{1.09}$Cl$_6$ SSE shows poor chemical stability toward Li metal (fig. S18, see the Supplementary Materials) and tends to decompose into Ho metal or Li-Ho alloy and LiCl at the Li metal interface according to the Ho L$_3$-edge and Cl K-edge XANES (fig. S18, C and D). Time-dependent electrochemical impedance spectroscopy (EIS) of the Li/Li$_{2.73}$Ho$_{1.09}$Cl$_6$/Li cell shows gradually increasing impedance after contact between the SSE and Li metal after 60 hours, and the Li metal turns black after 30 hours, suggesting the continuous formation of interface with lower ionic conductivity (fig. S18A, see the Supplementary Materials). In addition, as shown in fig. S18E, the overpotential of symmetric all–solid-state Li/Li$_{2.73}$Ho$_{1.09}$Cl$_6$/Li cell undergoes gradual increase during the initial 20 hours and then decrease after 600 hours, which confirms the continuous decomposition of Li$_{2.73}$Ho$_{1.09}$Cl$_6$ at first, followed by

lithium dendrite growth in the grain boundaries. In sharp contrast, the time-dependent EIS of the Li/Li$_9$N$_2$Cl$_3$/Li cell remains almost unchanged for 60 hours, and the Li metal retains its lustrous metal color with residual this vacancy-rich Li$_9$N$_2$Cl$_3$ powder on the surface after 30 hours (fig. S18B, see the Supplementary Materials). The compatibility of Li$_{2.73}$Ho$_{1.09}$Cl$_6$ toward the vacancy-rich Li$_9$N$_2$Cl$_3$ SSE was also confirmed by the time-dependent EIS and N K-edge and Ho L$_3$-edge XANES as shown in fig. S17 (B to D) (see the Supplementary Materials). The time-dependent EIS of the of thin Li$_9$N$_2$Cl$_3$ layer–Li$_{2.73}$Ho$_{1.09}$Cl$_6$–thin Li$_9$N$_2$Cl$_3$ layer (LNC-LHC-LNC) SSE layers maintains stable for 60 hours. In addition, the N K-edge and Ho L$_3$-edge XANES spectra of the mixture of Li$_9$N$_2$Cl$_3$ and Li$_{2.73}$Ho$_{1.09}$Cl$_6$ present no obvious change compared to that pure Li$_9$N$_2$Cl$_3$ and Li$_{2.73}$Ho$_{1.09}$Cl$_6$, respectively. Therefore, all–solid-state lithium metal batteries are demonstrated next with a configuration of the LNC-LHC-LNC as the SSE.

Figure 5 presents the voltage profiles of a Li-LNC-LHC-LNC-Li symmetric all–solid-state cell (small-area pellet type; size, 0.785 cm$^2$) during Li-stripping and Li-plating processes at 0.1 mA/cm$^2$ and 0.1 mAh/cm$^2$. This cell is constructed with one LHC (weight, 100 mg; thickness, approximately 0.45 mm) SSE layer and two LNC (weight, 5 mg; thickness, approximately 0.05 mm) layers. The symmetric cell shows steady overpotential of around 50 to 60 mV, and no unexpected overpotential change related to short circuit is observed over 3000 cycles. In addition, tested with a step increase in current density and a fixed stripping/plating time of 1 hour, the lithium symmetric cell demonstrated consistent potential profiles and impedance within a threshold of 10 mA/cm$^2$ and 10 mAh/
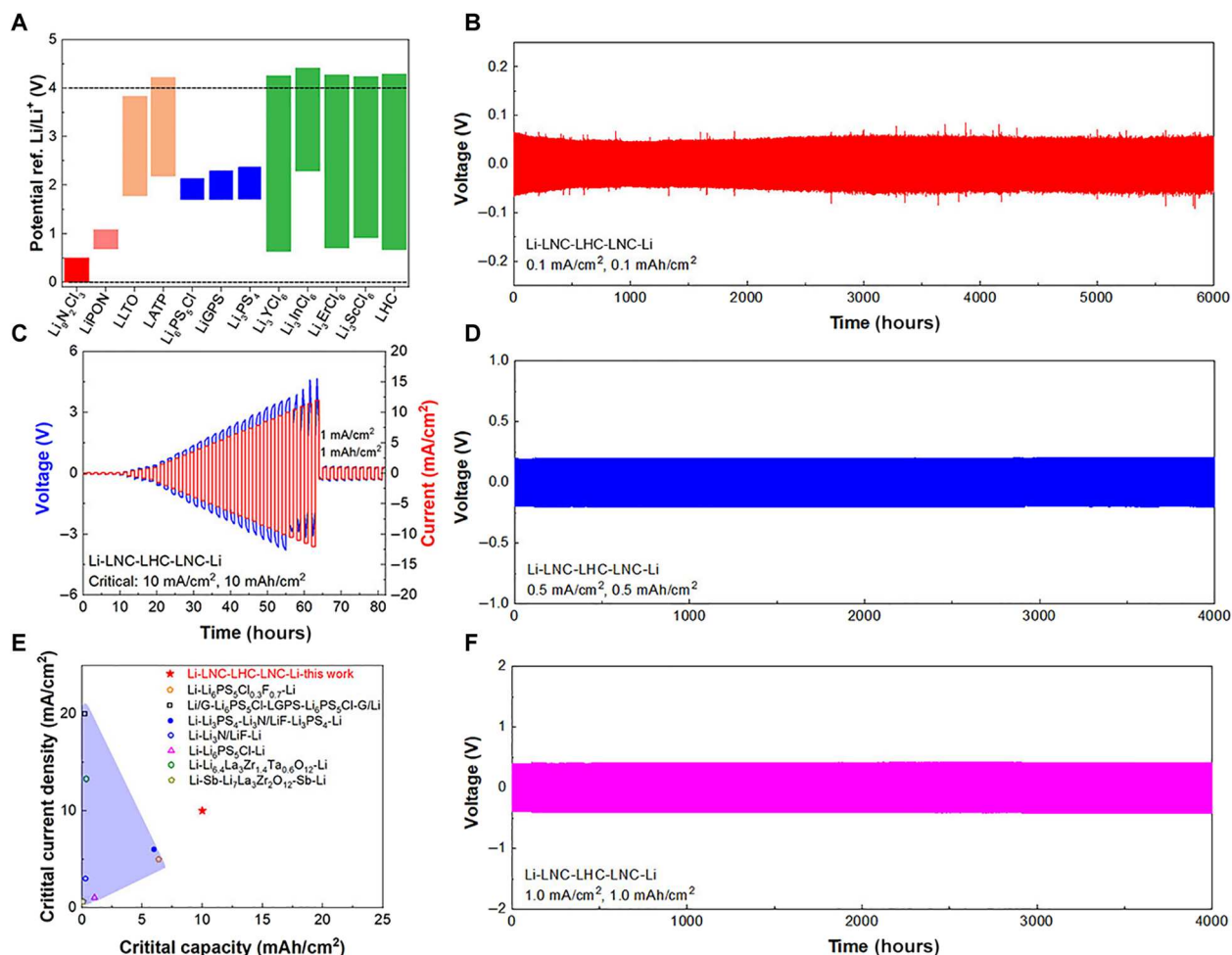
**Fig. 5. Investigation of all–solid-state lithium symmetric cells.** (**A**) Calculated thermodynamics intrinsic electrochemical windows of this vacancy-rich $Li_9N_2Cl_3$ SSE and other common SSEs, including nitrides, oxides, sulfides, and halides. Voltage profiles of Li-LNC-LHC-LNC-Li symmetric all–solid-state cell (LNC, 5 mg for each layer; LHC, 100 mg) with (**B**) a current density of 0.1 mA/cm$^2$ and a fixed capacity of 0.1 mAh/cm$^2$ and (**C**) step-increased current densities and capacity (fixed 1 hour time for Li plating/stripping). Voltage profiles of Li-LNC-LHC-LNC-Li symmetric all–solid-state cell (LNC, 5 mg for each layer; LHC, 100 mg) with (**D**) a current density of 0.5 mA/cm$^2$ and a fixed capacity of 0.5 mAh/cm$^2$. (**E**) Comparison of CCDs and capacity between this work and other reports of sulfide, oxide, and nitride solid-state electrolytes: Li-Li$_6$PS$_5$Cl$_{0.3}$F$_{0.7}$-Li (56), Li/G-Li$_6$PS$_5$Cl-LGPS-Li$_6$PS$_5$Cl-G/Li (57), Li-Li$_3$PS$_4$-Li$_3$N/LiF-Li$_3$PS$_4$-Li (58), Li-Li$_3$N/LiF-Li (58), Li-Li$_6$PS$_5$Cl-Li (59), Li-Li$_{6.4}$La$_3$Zr1.4Ta$_{0.6}$O12-Li (60), and Li-Sb-Li$_7$La$_3$Zr$_2$O$_{12}$-Sb-Li (61). Voltage profiles of Li-LNC-LHC-LNC-Li symmetric all–solid-state cell (LNC, 5 mg for each layer; LHC, 100 mg) with (**F**) a current density of 1.0 mA/cm$^2$ and a fixed capacity of 1.0 mAh/cm$^2$.

cm$^2$, as depicted in Fig. 5 and figs. S19 and S20 (see the Supplementary Materials). However, when the current density ascended to a range of 10.5 to 12 mAh/cm$^2$, the lithium symmetric cell exhibited a precipitous decline in overpotential and impedance, an indication of lithium dendrite proliferation, yet devoid of internal short circuit. When the current density returned to 1 mA/cm$^2$, the lithium symmetric cells demonstrated stable cycling with a steadily decreasing overpotential. This indicates continued lithium dendrite growth due to interface damage from exceeding the CCD of 10 mA/cm$^2$. Figure 5 summarizes the comparison with reported all–solid-state lithium symmetric cells using sulfides, nitrides, or oxides. The Li-LNC-LHC-LNC-Li symmetric cell presents a breakthrough in terms of CCDs and lithium-stripping/plating capacity. To achieve the target of high areal capacity, the lithium-stripping/plating behavior under higher current densities was tested at 0.5 and 1 mA/cm$^2$ with a fixed stripping/plating time of 1 hour, as shown in Fig. 5.

The Li-LNC-LHC-LNC-Li symmetric cell displays long-term stable lithium-stripping/plating cycling for over 2000 cycles at 0.5 mA/cm$^2$ and 0.5 mAh/cm$^2$ and over 2000 cycles at 1 mA/cm$^2$ and 1 mAh/cm$^2$. To further demonstrate the capability of $Li_9N_2Cl_3$ SSE to stabilize lithium metal, the Li-LNC-Li symmetric all–solid-state cells (small-area pellet type; size, 0.785 cm$^2$) also display stable Li-stripping and Li-plating processes up to 10 mA/cm$^2$ and 10 mAh/cm$^2$ and long-term stable lithium-stripping/plating cycling for 2000 cycles at 0.1 mA/cm$^2$ and 0.1 mAh/cm$^2$ and at 1 mA/cm$^2$ and 1 mAh/cm$^2$ (figs. S16, B to D, see the Supplementary Materials). In addition, compared to commercial LiCl, LiI, and Li$_3$N, this $Li_9N_2Cl_3$ SSE demonstrates much more stable lithium-stripping and lithium-plating processes (LiCl and LiI, not available for lithium-stripping and lithium-plating processes at 0.1 mA/cm$^2$ and 0.1 mAh/cm$^2$ due to low ionic conductivity; Li$_3$N, continuously decreasing

overpotential at 0.1 mA/cm$^2$ and 0.1 mAh/cm$^2$) (fig. S2, D to F, see the Supplementary Materials).

All–solid-state lithium metal batteries (small-area pellet type; size, 0.785 cm$^2$) were then demonstrated using Ni-rich LiNi$_{0.83}$Co$_{0.11}$Mn$_{0.06}$O$_2$ (NCM83) as cathode, LHC-LNC as the SSE (LHC: weight, 100 mg; thickness, approximately 0.45 mm; LNC: weight, 10 mg; thickness, approximately 0.1 mm) and lithium metal as anode, giving the NCM83-LHC-LNC-Li configuration as shown in fig. S21 (see the Supplementary Materials). The solid sections reveal a firm contact between each layer, including the LHC, LNC, and cathode layers. Figure 6 presents the voltage profiles of full cells with a capacity loading of 4.46 mg/cm$^2$, cycled at 0.1 C (where 1 C = 200 mA/g) between 2.7 and 4.3 V versus Li$^+$/Li at room temperature (25°C). The corresponding areal current density of 0.1 C, approximately 0.0892 mA/cm$^2$, is near to 0.1

mA/cm$^2$. This value is lower than the CCD of lithium symmetric cells, thereby mitigating the risk of lithium dendrite formation as shown in tables S16 and S17 (see the Supplementary Materials). The initial reversible capacity is 208.2 mAh/g with a high initial CE of ~89.3% when cycled 0.1 C. In the following cycles, the CE reaches nearly 100%. Rate performance was tested with cycling rates up to 1.0 C to demonstrate the stability toward lithium metal and the suppression of lithium dendrites by this vacancy-rich Li$_9$N$_2$Cl$_3$ in full cells at high current densities (Fig. 6). When cycled at 0.2, 0.4, 0.5, and 1.0 C, the full cells displayed smooth voltage profiles, which indicated no lithium dendrite growth in the SSE layers. The long-term stability of Li$_9$N$_2$Cl$_3$ toward lithium metal in full cells was also confirmed by long cycling at 0.1 and 0.5 C (Fig. 6). As shown in Fig. 6, the full cell delivered stable capacity retention of 87.98% with 183 mAh/g after 250 cycles when
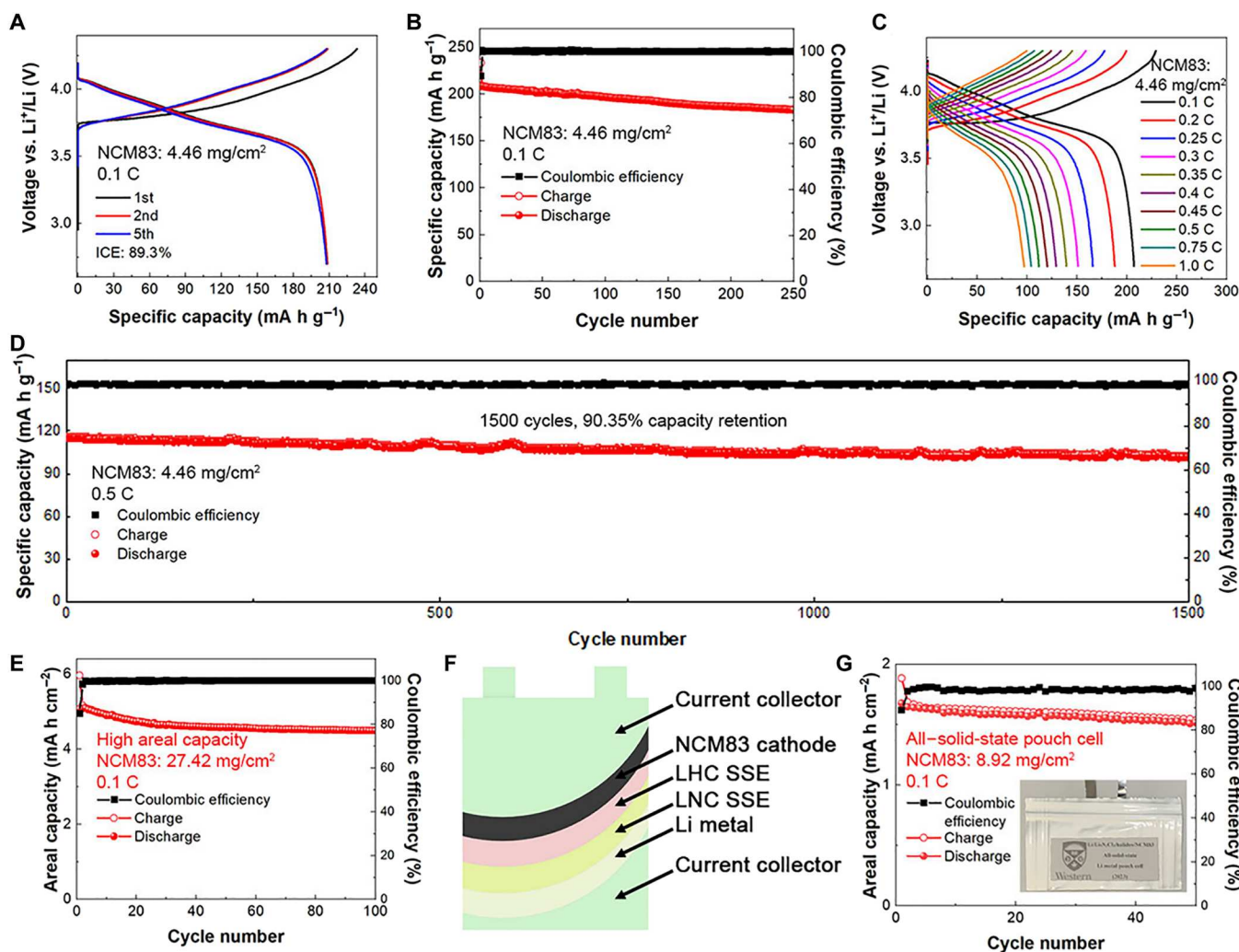


**Fig. 6. Investigation of all–solid-state lithium batteries.** Long-term electrochemical performance of the NCM83-LHC-LNC-Li all–solid-state lithium metal batteries at 25°C with an operating voltage window between 4.3 and 2.7 V and the cathode loading of 4.46 mg/cm$^2$. (**A**) The charge/discharge curves at 0.1 C. (**B**) Charge-discharge capacity and the CE as a function of cycle number for all–solid-state lithium metal batteries cycled at 0.1 C. (**C**) The charge/discharge curves at incremental cycling rates up to 1.0 C. (**D**) Charge-discharge capacity and the CE as a function of cycle number for all–solid-state lithium metal batteries cycled at 0.5 C. High-loading all–solid-state lithium metal batteries performance (areal loading of NMC83, 27.42 mg/cm$^2$; initial reversible areal capacity, 5.16 mAh/cm$^2$). (**E**) The charge-discharge capacity and CE as a function of cycle number. (**F**) Schematic and (**G**) charge-discharge capacity and CE as a function of cycle number of an all–solid-state lithium metal pouch cell with a high areal capacity (initial reversible areal capacity, 1.67 mAh/cm$^2$). ICE, initial Coulombic efficiency.

cycled at 0.1 C. At a higher current density of 0.5 C, it demonstrated extremely stable long-term cycling with capacity retention of 90.35% and reversible capacity of 103 mAh/g over 1500 cycles (see Fig. 6). Given the economic constraints imposed by the utilization of the Ho element, it becomes imperative to resort to other conventional SSEs for cathode materials, such as commercially accessible sulfide SSEs. All–solid-state lithium metal batteries, configured as NCM83-$Li_6PS_5Cl$-LNC-Li, have demonstrated impressive electrochemical stability at both 0.1 and 0.5 C. Specifically, these cells exhibit a high capacity retention of 96.43% with an energy capacity of 201.5 mAh/g over 50 cycles at 0.1 C and 95.01% capacity retention with an energy capacity of 107.7 mAh/g over an extended 350 cycles at 0.5 C as shown in fig. S22 (see the Supplementary Materials). To circumvent potential interfacial reactivity between NMC83 and $Li_6PS_5Cl$, we strategically coated NMC83 cathode particles with protective $LiNbO_x$ layers, with a thickness of approximately 5 nm, using the atomic layer deposition technique (45).

To effectively demonstrate the potential for long driving range in EV applications, it is crucial to increase the areal capacity to at least 3 mAh/cm$^2$ and develop all–solid-state lithium metal pouch cells (3, 46). To achieve this target of the areal capacity, we increase the NMC83 cathode loading to 27.42 mg/cm$^2$, as shown in Fig. 6 and fig. S23 (see the Supplementary Materials). When cycled at 0.1 C, the cell delivered a high reversible areal capacity of 5.16 mAh/cm$^2$ and a specific capacity was 188.14 mAh/g. The cell delivered good cycling stability with high reversible areal capacity (4.49 mAh/cm$^2$ over 100 cycles) and high capacity retention (86.91% over 100 cycles). In addition, all–solid-state lithium metal pouch cells have also been demonstrated by adopting dry-film processes (see Fig. 6) (47). A NCM83 cathode film (a mixture of NCM83 and $Li_{2.73}Ho_{1.09}Cl_6$ with cathode loading of 8.92 mg/cm$^2$), $Li_{2.73}Ho_{1.09}Cl_6$ (100 μm in thickness), and vacancy-rich $Li_9N_2Cl_3$ (100 μm in thickness) SSE thin films have been prepared as shown in fig. S24 (see the Supplementary Materials) and assembled into all–solid-state lithium metal pouch cells. This pouch cell delivered high initial capacity of 1.67 mAh/cm$^2$ and maintained 1.52 mAh/cm$^2$ after 50 cycles at 0.1 C (see Fig. 6). To further amplify the areal capacity of the pouch cell for practical application, all–solid-state lithium metal pouch cells with a heightened cathode loading of 27.42 mg/cm$^2$ were prepared as shown in fig. S25 (see the Supplementary Materials). These exhibited a high initial areal capacity of 4.8 mAh/cm$^2$, which was maintained at 4.27 mAh/cm$^2$ after 50 cycles at 0.05 C. This stable cycling performance of all–solid-state lithium metal configuration suggests the excellent compatibility of this vacancy-rich $Li_9N_2Cl_3$ SSE with the lithium metal anode.

Regarding practical all–solid-state lithium metal batteries, the enhancement of the CCD in all–solid-state lithium symmetric cells to 10 mA/cm$^2$ and 10 mAh/cm$^2$ is a substantial breakthrough that has the potential to unlock higher energy density and faster charging capabilities. However, there are still some limitations of this vacancy-rich $Li_9N_2Cl_3$ for all–solid-state lithium metal batteries, particularly at high current densities. The high resistance of overall SSE layers in the lithium symmetric cells results in high overpotential as shown in table S16 (see the Supplementary Materials). For instance, the LHC layer (weight, 100 mg; thickness, ~0.45 mm) has a resistance of approximately 200 ohms, while each LNC layer (weight, 5 mg; thickness, ~0.05 mm) has a resistance of around 140 ohms. Cumulatively, the LNC-LHC-LNC layer (thickness, 0.55

mm) results in a resistance of about 500 ohms. This high overpotential compromises the capacity and energy density, rendering them unacceptable for practical batteries and could even lead to negligible capacity, as seen in the high overpotential (~3.7 V) of the lithium symmetric cells at 10 mA/cm$^2$.

It is evident that full cells with a capacity loading of 4.46 mg/cm$^2$ exhibit low overpotential, delivering a high capacity of ~208 mAh/g and good cycling at 0.1 C (0.0892 mA/cm$^2$). However, when the current density is raised to 1.0 C (0.892 mA/cm$^2$), the full cells only provide around 100 mAh/g. This underscores the point that the high overpotential arising from the notable resistance of the SSE layers can constrain the capacity and energy density at elevated current densities, especially for fast charging applications. In light of these findings, it seems plausible to use thin LNC layers and other cathode-compatible SSEs with high ionic conductivity [e.g., $Li_{10}GeP_2S_{12}$; (48); room-temperature ionic conductivity, 12 mS/cm] to help enhance the electrochemical performance at high current densities.

## DISCUSSION

In summary, this study presents the vacancy-rich $Li_9N_2Cl_3$, an SSE demonstrating high lithium compatibility and dry-air stability. Compared to earlier research on $Li_9N_2Cl_3$ (21, 22, 28, 49), our study offers a more extensive analysis and innovative advancements in the understanding of its structure, synthesis, lithium-ion diffusion mechanisms, and electrochemical performance as shown in table S18 (see the Supplementary Materials). A lattice and vacancy-driven lithium-ion migration mechanism, corroborated via SXRD, PDF, TOF neutron diffraction, DFT calculation, and AIMD simulation, is central to its superior functionality. Notably, this SSE exhibits a room-temperature ionic conductivity an order of magnitude higher ($4.3 \times 10^{-5}$ S/cm) than previous records (~$1 \times 10^{-6}$ S/cm), with an activation energy of 0.378 eV. Operando studies [operando SXRD and XANES studies with low-angle (3°) incidence x-ray] and theoretical calculations shed light on its intrinsic stability toward lithium metal, effectively preventing lithium-SSE interfacial reaction and dendrite formation. These features underpin its utility in high-performance all–solid-state lithium symmetric cells and lithium metal batteries, capable of achieving high CCDs and lithium-stripping/plating capacity of 10 mA/cm$^2$ and 10 mAh/cm$^2$, respectively. Furthermore, these cells display ultrastable cycling over 2000 cycles at various densities (0.1, 0.5, and 1.0 mAh/cm$^2$) with a fixed lithium-stripping/plating time of 1 hour. The vacancy-rich Li9N2Cl3 SSE's impressive dry-air stability and excellent performance in battery dry rooms cement its potential for practical applications in modern battery industries. The excellent stability of vacancy-rich $Li_9N_2Cl_3$ toward lithium metal produced high-performance all–solid-state lithium symmetric cells and all–solid-stable lithium metal batteries. Because of the high lithium compatibility of this vacancy-rich $Li_9N_2Cl_3$, all–solid-state lithium metal batteries with Ni-rich NCM83, in the configuration NCM83-LHC-LNC-Li, delivered excellent electrochemical performance with long cycling life at low and high current densities (87.98% capacity retention with 183 mAh/g over 250 cycles at 0.1 C and 90.35% capacity retention with 103 mAh/g over 1500 cycles at 0.5 C). Moreover, these cells enable high areal capacity of ~5 mAh/cm$^2$ (cathode loading of 27.42 mg/cm$^2$) for small-area pellet type cells (size, 0.785 cm$^2$; thickness of SSE layers, 0.55 mm) and 4.8 mAh/

cm$^2$ (cathode loading of 27.42 mg/cm$^2$) for all–solid-state lithium metal pouch cells (size, 2 × 2.5 cm$^2$; thickness of SSE layers, 200 μm). Our findings establish the vacancy-rich Li$_9$N$_2$Cl$_3$ as a high-performance SSE demonstrating exceptional stability toward lithium metal anodes, essential for achieving high–areal capacity and longevity in all–solid-state lithium metal batteries. As such, this SSE presents a viable candidate for addressing the escalating demands of the rapidly evolving EV market.

## MATERIALS AND METHODS

### Preparation of the Li$_9$N$_2$Cl$_3$ SSE through ball-milling method

Lithium nitride (Li$_3$N; Alfa Aesar, 99.4%) and lithium chloride (LiCl; Alfa Aesar, 99.9%) were weighed to the stoichiometric molar ratio. The mixtures were mechanically mixed in a ZrO$_2$ pot with ZrO$_2$ balls (φ = 5 mm, the mass ratio of balls to mixtures was 40). The mixing process was performed using a planetary ball-milling apparatus. All the preparation processes were carried out with an Ar atmosphere.

### Characterizations

Powder XRD patterns were collected on a Bruker AXS D8 Advance with a Cu Kα radiation (λ = 1.54178 Å) with a special holder to avoid exposure to air during test. The morphology was characterized with by a Hitachi S-4800 field-emission SEM for SEM and energy-dispersive x-ray spectroscopy mapping.

### Nanoindentation tests

In situ Berkovich indentation tests were performed on an Alemnis Nano indenter within an Apreo-2S field-emission gun SEM, controlled by AMICS software. Tests were conducted under vacuum at room temperature to maintain environmental consistency. Five indentations were performed per sample, ensuring indenter placement away from residual surface particles via SEM. The indenter was programmed for a constant displacement rate of 5 nm/s, reaching a total indentation displacement of 9 μm. After attaining maximum displacement, a dwell time of 5 s was implemented before retraction. SEM imaging parameters were set to a 20-keV electron beam energy, a 6.4-nA beam current, and a 25-mm working distance.

### Solid-state NMR measurements

Variable temperature spin-lattice relaxation time ($T_1$) was measured on the same machine as our previous work [Nano Energy 69 (2020) 104396, Energy Storage Materials 30 (2020) 238–249]. The $^7$Li Larmor frequency was 155.248 MHz, and the π/2 and π pulse lengths were determined to be 2.1 and 4.4 μs, respectively. Chemical shifts were referenced with respect to a 1.0 M LiCl solution. Spectra were acquired in the temperature range of 20° to 150°C. The $^7$Li spin-lattice relaxation times ($T_1$) were determined using an inversion-recovery NMR method where the experimental data were fit to a three-parameter inversion-recovery equation using the Chemagnetics Spinsight NMR software package.

### Synchrotron-based x-ray powder diffraction, x-ray total scattering and XANES

The synchrotron-based x-ray powder diffraction and x-ray total scattering were carried out at the Very Sensitive Elemental and Structural Probe Employing Radiation from a Synchrotron and Brockhouse X-ray Diffraction and Scattering-High Energy Wiggler Beamline beamlines at the Canadian Light Source. The N K-, Cl K-, and Ho L$_3$-edge XANES spectra were collected at the Spherical Grating Monochromator (SGM) beamline and Soft X-ray Microcharacterization Beamline at the Canadian Light Source. X-ray FLY mode was used to collect the XANES spectra.

### Neutron total scattering

The room-temperature neutron diffraction was performed at the Nanoscaled Ordered Materials Diffractometer (NOMAD) beamline (BL-1B) at the Spallation Neutron Source at Oak Ridge National Laboratory. Powdered (~0.15-g) samples were packed into 3-mm quartz capillaries and sealed with epoxy in a glove box filled with dry argon. The acquisition time was 1 hour for each sample. The background was subtracted from the acquired data followed by normalization against the vanadium rod.

### Ionic conductivity measurements

Ionic conductivities were measured by ac impedance spectroscopy. Typically, powder samples were placed between two stainless steel rods with 10-mm diameter and pressed at 3 tonnes (~380 MPa). The thickness of the pellet was between 0.8 and 1.0 mm depending on the amount of powder sample used. The procedures were performed inside an Ar-filled glove box. EIS was performed with in the temperature range −5° to 75°C using versatile multichannel potentiostat 3/Z (VMP3) from 7 MHz to 1 Hz with an amplitude of 10 mV.

### Electrochemical characterizations

All the cell preparation processes were conducted inside an Ar-filled glove box with the in-house fabricated all–solid-state cells (fig. S26). For Li-Li$_9$N$_2$Cl$_3$-Li$_{2.73}$Ho$_{1.09}$Cl$_6$-Li$_9$N$_2$Cl$_3$-Li symmetric cells, ~100 mg of Li$_{2.73}$Ho$_{1.09}$Cl$_6$ and 5 mg of Li$_9$N$_2$Cl$_3$ were placed into a polytetrafluoroethylene (PTFE) die with diameter of 10 mm and pressed at 3 tonnes. Then, two lithium foils (diameter, 10 mm; thickness, 250 μm) were attached to both sides of the SSE layers. For the Li-Li$_9$N$_2$Cl$_3$-Li symmetric all–solid-state cells, 20 mg was placed into a PTFE die with diameter of 10 mm and pressed at 3 tonnes as the SSE layer. Then, two lithium foils (diameter, 10 mm; thickness, 250 μm) were attached to both sides of the SSE layers. For cathode composites fabrication, commercial Ni-rich LiNi$_{0.83}$Co$_{0.11}$Mn$_{0.06}$O$_2$ (NCM83) cathodes and as-prepared Li$_{2.73}$Ho$_{1.09}$Cl$_6$ were hand-milled for 5 min with weight ratio of 70:30 without carbon additives. For Li/Li$_9$N$_2$Cl$_3$/Li$_{2.73}$Ho$_{1.09}$Cl$_6$/NCM83 full-cell fabrication, ~100 mg of Li$_{2.73}$Ho$_{1.09}$Cl$_6$ powder was placed into a PTFE die with diameter of 10 mm and pressed at 3 tonnes. Subsequently, 5 mg of the cathode composite powder was dispersed on one side of the electrolyte and pressed again at 3 tonnes. Before attaching lithium metal anode (diameter, 10 mm; thickness, 250 μm) on the other side of the electrolyte layer, a thin layer of Li$_9$N$_2$Cl$_3$ (10 mg) was set to face lithium metal anode. For Li/Li$_9$N$_2$Cl$_3$/Li$_6$PS$_5$Cl/NCM83 full-cell fabrication, ~100 mg of Li$_6$PS$_5$Cl powder was placed into a PTFE die with diameter of 10 mm and pressed at 3 tonnes. Subsequently, 5 mg of the cathode composite powder was dispersed on one side of the electrolyte and pressed again at 3 tonnes. Before attaching lithium metal anode (diameter, 10 mm; thickness, 250 μm) on the other side of the electrolyte layer, a thin layer of Li$_9$N$_2$Cl$_3$ (10 mg) was set to face lithium metal anode. The full cells were cycled in

the voltage range of 2.7 to 4.3 V (versus Li$^+$/Li) without external stack pressure using a Neware battery test system (Shenzhen, China) and a Land cycler (Wuhan, China) at room temperature. The galvanostatic charge-discharge studies of NCM83 cathodes were conducted at different current densities.

### All–solid-state lithium metal pouch cells
All the cell preparation processes were conducted inside an Ar-filled glove box. Dry-film processes were used to prepare SSEs and cathode films (47). Then, SSEs and cathode films and lithium metal foils were stacked together to form pouch cells, sealed with aluminium bags under vacuum.

### Computation
#### DFT calculation
All the calculations are carried out using Vienna Ab initio Simulation Package (50) based on DFT. The projector augmented-wave (51) approach and generalized gradient approximation of Perdew-Burke-Ernzerhof functional (52) were used for the energy calculations. The plane-wave energy cutoff and k-points density used in the calculations were consistent with that of Materials Project (53).

#### Structural ordering
The Li$_9$N$_2$Cl$_3$ has a cubic anti-fluorite structure with space group of $Fm\bar{3}m$. In the anti-fluorite structure, Li partially occupied the tetrahedral 8c sites, and N and Cl co-occupied the vertex 4a sites. To determine the atomistic configurations of disordered structure, we performed the structural ordering as our previous works (11, 31). On the basis of experimental refined structure, we used a 2 × 2 × 2 supercell model with a formula of Li$_{54}$N$_{12}$Cl$_{18}$ to generate a total of 50 symmetrically distinctive structures, of which 30 structures were generated by minimizing the electrostatic energies from three thousands of random configurations and the other 20 were generated by randomizing the disordered occupancies. All the structures were statically relaxed in the DFT calculations, and the structure with lowest energy was identified as the ground state structure for other calculations.

#### Li vacancy formation energy
We calculated vacancy formation energy for each single Li in the ordered supercell model of Li$_{54}$N$_{12}$Cl$_{18}$. A single neutral Li atom was removed the supercell, and, then, the formation energy of Li vacancy at different sites was calculated as

$$\Delta E_{\text{vac}} = E[\text{Li}_{53}\text{N}_{12}\text{Cl}_{18}] + E[\text{Li}] - E[\text{Li}_{54}\text{N}_{12}\text{Cl}_{18}]$$

where $E[\text{Li}_{54}\text{N}_{12}\text{Cl}_{18}]$ represents the total energies of the pristine supercell, $E[\text{Li}_{53}\text{N}_{12}\text{Cl}_{18}]$ represents the defected supercell with a single Li vacancy, and $E[\text{Li}]$ is the energy of Li metal. Similarly, the Li vacancy formation energy is calculated in LiCl and β-Li$_3$N as comparison. The supercell model of LiCl (32 formula units and a total of 64 atoms) and β-Li$_3$N (36 formula units and a total of 144 atoms) is used.

#### AIMD simulation
We performed AIMD simulations in the supercell model of Li$_{54}$N$_{12}$Cl$_{18}$ using NVT ensemble with Nosé-Hoover thermostat (33). Non-spin mode, time step of 2 fs, and Γ-centered k-point were used. In each simulation, structures were first heated from 100 K to the target temperatures (600 to 100 K) at a constant rate during a period of 2 ps. Then, the AIMD simulations last from 80 to 300 ps until the ionic diffusivity converged with a relative standard deviation

between 20 and 30% according to our work (34). The ionic diffusivity D was calculated as the mean square displacement over the time interval Δt

$$D = \frac{1}{2Nd\Delta t} \sum_{i=1}^{N} \langle [\boldsymbol{r}_i(t + \Delta t) - \boldsymbol{r}_i(t)]^2 \rangle_t$$

where $d = 3$ is the dimension of the diffusion, N is the total number of diffusion ions, $\boldsymbol{r}_i(t)$ is the displacement of the ith ion at time t. The ionic conductivity was calculated according to the Nernst-Einstein relationship

$$\sigma = \frac{nq^2}{k_{\text{B}}T} D$$

where n is the mobile ions volume density and q is the ionic charge. Arrhenius relation is used to get activation energy and to extrapolate ionic conductivity at desired temperature

$$\sigma T = \sigma_0 \exp\left(\frac{-E_{\text{a}}}{k_{\text{B}}T}\right)$$

where $E_{\text{a}}$ is activation energy and $\sigma_0$ is the pre-exponential factor.
#### Electrochemical window
The phase equilibria were evaluated along the energy minimum using the decomposition energy $\Delta E_{\text{D}}$ with the chemical potential $\mu_{\text{Li}}$ referenced to Li metal in the previous studies (54, 55). The decomposition reaction energy at a given chemical potential $\mu_{\text{Li}}$ of element Li is calculated as

$$\Delta E_{\text{D}}^{\text{open}}(\text{phase}, \mu_{\text{Li}}) = E_{\text{eq}}[C_{\text{eq}}(C, \mu_{\text{Li}})] - E(\text{phase}) - \Delta n_{\text{Li}} \cdot \mu_{\text{Li}}$$

where $C_{\text{eq}}(C, \mu_{\text{Li}})$ is the phase equilibria of a given phase composition C at the given chemical potential.

### Supplementary Materials
This PDF file includes:
Figs. S1 to S26
Tables S1 to S18

### REFERENCES AND NOTES
1. J. B. Goodenough, K.-S. Park, The Li-ion rechargeable battery: A perspective. *J. Am. Chem. Soc.* **135**, 1167–1176 (2013).
2. J. Liu, Z. Bao, Y. Cui, E. J. Dufek, J. B. Goodenough, P. Khalifah, Q. Li, B. Y. Liaw, P. Liu, A. Manthiram, Y. S. Meng, V. R. Subramanian, M. F. Toney, V. V. Viswanathan, M. S. Whittingham, J. Xiao, W. Xu, J. Yang, X.-Q. Yang, J.-G. Zhang, Pathways for practical high-energy long-cycling lithium metal batteries. *Nat. Energy* **4**, 180–186 (2019).
3. P. Albertus, V. Anandan, C. Ban, N. Balsara, I. Belharouak, J. Buettner-Garrett, Z. Chen, C. Daniel, M. Doeff, N. J. Dudney, B. Dunn, S. J. Harris, S. Herle, E. Herbert, S. Kalnaus, J. A. Libera, D. Lu, S. Martin, B. D. McCloskey, M. T. McDowell, Y. S. Meng, J. Nanda, J. Sakamoto, E. C. Self, S. Tepavcevic, E. Wachsman, C. Wang, A. S. Westover, J. Xiao, T. Yersak, Challenges for and pathways toward Li-metal-based all-solid-state batteries. *ACS Energy Lett.* **6**, 1399–1404 (2021).
4. Y.-G. Lee, S. Fujiki, C. Jung, N. Suzuki, N. Yashiro, R. Omoda, D.-S. Ko, T. Shiratsuchi, T. Sugimoto, S. Ryu, J. H. Ku, T. Watanabe, Y. Park, Y. Aihara, D. Im, I. T. Han, High-energy long-cycling all-solid-state lithium metal batteries enabled by silver–carbon composite anodes. *Nat. Energy* **5**, 299–308 (2020).
5. A. Sarkar, I. C. Nlebedim, P. Shrotriya, Performance degradation due to anodic failure mechanisms in lithium-ion batteries. *J. Power Sources* **502**, 229145 (2021).
6. K. Xu, Nonaqueous liquid electrolytes for lithium-based rechargeable batteries. *Chem. Rev.* **104**, 4303–4418 (2004).
7. S. Xia, X. Wu, Z. Zhang, Y. Cui, W. Liu, Practical challenges and future perspectives of all-solid-state lithium-metal batteries. *Chem* **5**, 753–785 (2019).

8. J. Schnell, T. Günther, T. Knoche, C. Vieider, L. Köhler, A. Just, M. Keller, S. Passerini, G. Reinhart, All-solid-state lithium-ion and lithium metal batteries–paving the way to large-scale production. *J. Power Sources* **382**, 160–175 (2018).

9. J. Hu, Z. Yao, K. Chen, C. Li, High-conductivity open framework fluorinated electrolyte bonded by solidified ionic liquid wires for solid-state Li metal batteries. *Energy Storage Mater.* **28**, 37–46 (2020).

10. W. D. Richards, L. J. Miara, Y. Wang, J. C. Kim, G. Ceder, Interface stability in solid-state batteries. *Chem. Mater.* **28**, 266–273 (2016).

11. S. Wang, Q. Bai, A. M. Nolan, Y. Liu, S. Gong, Q. Sun, Y. Mo, Lithium chlorides and bromides as promising solid-state chemistries for fast ion conductors with good electrochemical stability. *Angew. Chem. Int. Ed.* **58**, 8039–8043 (2019).

12. X. Liu, R. Garcia-Mendez, A. R. Lupini, Y. Cheng, Z. D. Hood, F. Han, A. Sharafi, J. C. Idrobo, N. J. Dudney, C. Wang, C. Ma, J. Sakamoto, M. Chi, Local electronic structure variation resulting in Li 'filament' formation within solid electrolytes. *Nat. Mater.* **20**, 1485–1490 (2021).

13. S. Yu, D. J. Siegel, Grain boundary softening: A potential mechanism for lithium metal penetration through stiff solid electrolytes. *ACS Appl. Mater. Interfaces* **10**, 38151–38158 (2018).

14. S. Wenzel, S. Randau, T. Leichtweiß, D. A. Weber, J. Sann, W. G. Zeier, J. Janek, Direct observation of the interfacial instability of the fast ionic conductor $Li_{10}GeP_2S_{12}$ at the lithium metal anode. *Chem. Mater.* **28**, 2400–2407 (2016).

15. B. Chen, J. Ju, J. Ma, J. Zhang, R. Xiao, G. Cui, L. Chen, An insight into intrinsic interfacial properties between Li metals and $Li_{10}GeP_2S_{12}$ solid electrolytes. *Phys. Chem. Chem. Phys.* **19**, 31436–31442 (2017).

16. X.-B. Cheng, C.-Z. Zhao, Y.-X. Yao, H. Liu, Q. Zhang, Recent advances in energy chemistry between solid-state electrolyte and safe lithium-metal anodes. *Chem* **5**, 74–96 (2019).

17. A. Banerjee, X. Wang, C. Fang, E. A. Wu, Y. S. Meng, Interfaces and interphases in all-solid-state batteries with inorganic solid electrolytes. *Chem. Rev.* **120**, 6878–6933 (2020).

18. S. Xin, Y. You, S. Wang, H.-C. Gao, Y.-X. Yin, Y.-G. Guo, Solid-state lithium metal batteries promoted by nanotechnology: Progress and prospects. *ACS Energy Lett.* **2**, 1385–1394 (2017).

19. T. Famprikis, P. Canepa, J. A. Dawson, M. S. Islam, C. Masquelier, Fundamentals of inorganic solid-state electrolytes for batteries. *Nat. Mater.* **18**, 1278–1291 (2019).

20. Y. Zhu, X. He, Y. Mo, Strategies based on nitride materials chemistry to stabilize Li metal anode. *Adv. Sci.* **4**, 1600517 (2017).

21. P. Hartwig, W. Weppner, W. Wichelhaus, A. Rabenau, Lithium nitride halides—New solid electrolytes with high $Li^+$ ion conductivity. *Angew. Chem. Int. Ed.* **19**, 74–75 (1980).

22. P. Hartwig, W. Weppner, W. Wichelhaus, Fast ionic lithium conduction in solid lithium nitride chloride. *Mater. Res. Bull.* **14**, 493–498 (1979).

23. J. Bates, N. Dudney, G. Gruzalski, R. Zuhr, A. Choudhury, C. Luck, J. Robertson, Electrical properties of amorphous lithium electrolyte thin films. *Solid State Ion.* **53**, 647–654 (1992).

24. Q. Yang, J. Hu, Z. Yao, J. Liu, C. Li, Durable $Li_2CN_2$ solid electrolyte interphase wired by carbon nanodomains via in situ interface lithiation to enable long-cycling Li metal batteries. *Adv. Funct. Mater.* **33**, 2206778 (2023).

25. H. Yamane, S. Kikkawa, M. Koizumi, Preparation of lithium silicon nitrides and their lithium ion conductivity. *Solid State Ion.* **25**, 183–191 (1987).

26. J. Li, C. Ma, M. Chi, C. Liang, N. J. Dudney, Solid electrolyte: The key for high-voltage lithium batteries. *Adv. Energy Mater.* **5**, 1401408 (2015).

27. W. Li, G. Wu, C. M. Araújo, R. H. Scheicher, A. Blomqvist, R. Ahuja, Z. Xiong, Y. Feng, P. Chen, $Li^+$ ion conductivity and diffusion mechanism in $\alpha$-$Li_3N$ and $\beta$-$Li_3N$. *Energ. Environ. Sci.* **3**, 1524–1530 (2010).

28. Y. Jia, J. Yang, Study of the lithium solid electrolytes based on lithium nitride chloride ($Li_9N_2Cl_3$). *Solid State Ion.* **96**, 113–117 (1997).

29. R. Marx, Preparation and crystal structure of lithium nitride chloride $Li_4NCl$. *J. Solid State Chem.* **128**, 241–246 (1997).

30. J. C. Bachman, S. Muy, A. Grimaud, H.-H. Chang, N. Pour, S. F. Lux, O. Paschos, F. Maglia, S. Lupart, P. Lamp, L. Giordano, Y. Shao-Horn, Inorganic solid-state electrolytes for lithium batteries: Mechanisms and properties governing ion conduction. *Chem. Rev.* **116**, 140–162 (2016).

31. X. He, Y. Mo, Accelerated materials design of $Na_{0.5}Bi_{0.5}TiO_3$ oxygen ionic conductors based on first principles calculations. *Phys. Chem. Chem. Phys.* **17**, 18035–18044 (2015).

32. J. Liang, X. Li, S. Wang, K. R. Adair, W. Li, Y. Zhao, C. Wang, Y. Hu, L. Zhang, S. Zhao, Site-occupation-tuned superionic $Li_xScCl_{3+x}$ halide solid electrolytes for all-solid-state batteries. *J. Am. Chem. Soc.* **142**, 7012–7022 (2020).

33. N. Shuichi, Constant temperature molecular dynamics methods. *Prog. Theor. Phys. Suppl.* **103**, 1–46 (1991).

34. X. He, Y. Zhu, A. Epstein, Y. Mo, Statistical variances of diffusional properties from ab initio molecular dynamics simulations. *NPJ Comput. Mater.* **4**, 18 (2018).

35. C. Li, L. Gu, J. Maier, Enhancement of the Li conductivity in LiF by introducing glass/crystal interfaces. *Adv. Funct. Mater.* **22**, 1145–1149 (2012).

36. D. E. Galvez-Aranda, J. M. Seminario, Ab initio study of the interface of the solid-state electrolyte $Li_9N_2Cl_3$ with a Li-metal electrode. *J. Electrochem. Soc.* **166**, A2048–A2057 (2019).

37. J. Sang, Y. Yu, Z. Wang, G. Shao, Theoretical formulation of $Li_{3a+b}N_aX_b$ (X = halogen) as a potential artificial solid electrolyte interphase (ASEI) to protect the Li anode. *Phys. Chem. Chem. Phys.* **22**, 12918–12928 (2020).

38. L. Cristofolini, Synchrotron X-ray techniques for the investigation of structures and dynamics in interfacial systems. *Curr. Opin. Colloid Interface Sci.* **19**, 228–241 (2014).

39. C. Gao, M. Liu, Instrumented indentation of fused silica by Berkovich indenter. *J. Non Cryst. Solids* **475**, 151–160 (2017).

40. A. Masias, N. Felten, R. Garcia-Mendez, J. Wolfenstine, J. Sakamoto, Elastic, plastic, and creep mechanical properties of lithium metal. *J. Mater. Sci.* **54**, 2585–2600 (2019).

41. R. Chen, Q. Li, X. Yu, L. Chen, H. Li, Approaching practically accessible solid-state batteries: Stability issues related to solid electrolytes and interfaces. *Chem. Rev.* **120**, 6820–6877 (2020).

42. W. Li, J. Liang, M. Li, K. R. Adair, X. Li, Y. Hu, Q. Xiao, R. Feng, R. Li, L. Zhang, Unraveling the origin of moisture stability of halide solid-state electrolytes by in situ and *operando* synchrotron X-ray analytical techniques. *Chem. Mater.* **32**, 7019–7027 (2020).

43. A. W. Gillespie, F. L. Walley, R. E. Farrell, T. Z. Regier, R. I. Blyth, Calibration method at the N K-edge using interstitial nitrogen gas in solid-state nitrogen-containing inorganic compounds. *J. Synchrotron Radiat.* **15** (Pt. 5), 532–534 (2008).

44. J. Liang, E. van der Maas, J. Luo, X. Li, N. Chen, K. R. Adair, W. Li, J. Li, Y. Hu, J. Liu, L. Zhang, S. Zhao, S. Lu, J. Wang, H. Huang, W. Zhao, S. Parnell, R. I. Smith, S. Ganapathy, M. Wagemaker, X. Sun, A series of ternary metal chloride superionic conductors for high-performance all-solid-state lithium batteries. *Adv. Energy Mater.* **12**, 2103921 (2022).

45. S. Deng, Q. Sun, M. Li, K. Adair, C. Yu, J. Li, W. Li, J. Fu, X. Li, R. Li, Insight into cathode surface to boost the performance of solid-state batteries. *Energy Storage Mater.* **35**, 661–668 (2021).

46. D. H. Tan, Y. S. Meng, J. Jang, Scaling up high-energy-density sulfidic solid-state batteries: A lab-to-pilot perspective. *Joule* **6**, 1755–1769 (2022).

47. C. Wang, R. Yu, H. Duan, Q. Lu, Q. Li, K. R. Adair, D. Bao, Y. Liu, R. Yang, J. Wang, Solvent-free approach for interweaving freestanding and ultrathin inorganic solid electrolyte membranes. *ACS Energy Lett.* **7**, 410–416 (2022).

48. N. Kamaya, K. Homma, Y. Yamakawa, M. Hirayama, R. Kanno, M. Yonemura, T. Kamiyama, Y. Kato, S. Hama, K. Kawamoto, A lithium superionic conductor. *Nat. Mater.* **10**, 682–686 (2011).

49. H. Sattlegger, H. Hahn, Über das system $Li_3N/LiCl$. *Z. Anorg. Allg. Chem.* **379**, 293–299 (1971).

50. G. Kresse, J. Furthmüller, Efficient iterative schemes for ab initio total-energy calculations using a plane-wave basis set. *Phys. Rev. B* **54**, 11169 (1996).

51. P. E. Blöchl, Projector augmented-wave method. *Phys. Rev. B* **50**, 17953–17979 (1994).

52. J. Heyd, G. E. Scuseria, Efficient hybrid density functional calculations in solids: Assessment of the Heyd–Scuseria–Ernzerhof screened Coulomb hybrid functional. *J. Chem. Phys.* **121**, 1187–1192 (2004).

53. A. Jain, S. P. Ong, G. Hautier, W. Chen, W. D. Richards, S. Dacek, S. Cholia, D. Gunter, D. Skinner, G. Ceder, Commentary: The Materials Project: A materials genome approach to accelerating materials innovation. *APL Mater.* **1**, 011002 (2013).

54. Y. Zhu, X. He, Y. Mo, First principles study on electrochemical and chemical stability of solid electrolyte–electrode interfaces in all-solid-state Li-ion batteries. *J. Mater. Chem. A* **4**, 3253–3266 (2016).

55. Y. Zhu, X. He, Y. Mo, Origin of outstanding stability in the lithium solid electrolyte materials: Insights from thermodynamic analyses based on first-principles calculations. *ACS Appl. Mater. Interfaces* **7**, 23685–23693 (2015).

56. F. Zhao, Q. Sun, C. Yu, S. Zhang, K. Adair, S. Wang, Y. Liu, Y. Zhao, J. Liang, C. Wang, Ultrastable anode interface achieved by fluorinating electrolytes for all-solid-state Li metal batteries. *ACS Energy Lett.* **5**, 1035–1043 (2020).

57. L. Ye, X. Li, A dynamic stability design strategy for lithium metal solid state batteries. *Nature* **593**, 218–222 (2021).

58. X. Ji, S. Hou, P. Wang, X. He, N. Piao, J. Chen, X. Fan, C. Wang, Solid-state electrolyte design for lithium dendrite suppression. *Adv. Mater.* **32**, 2002741 (2020).

59. G. Liu, W. Weng, Z. Zhang, L. Wu, J. Yang, X. Yao, Densified $Li_6PS_5Cl$ nanorods with high ionic conductivity and improved critical current density for all-solid-state lithium batteries. *Nano Lett.* **20**, 6660–6665 (2020).

60. H. Zheng, S. Wu, R. Tian, Z. Xu, H. Zhu, H. Duan, H. Liu, Intrinsic lithiophilicity of Li–Garnet electrolytes enabling high-rate lithium cycling. *Adv. Funct. Mater.* **30**, 1906189 (2020).

61. R. Dubey, J. Sastre, C. Cancellieri, F. Okur, A. Forster, L. Pompizii, A. Priebe, Y. E. Romanyuk, L. P. Jeurgens, M. V. Kovalenko, Building a better Li-garnet solid electrolyte/metallic Li interface with antimony. *Adv. Energy Mater.* **11**, 2102086 (2021).